Article

Aerodynamic Performance Analysis of Trailing Edge Serrations on a Wells Turbine

Abdullah Saad Alkhalifa, Mohammad Nasim Uddin (ID) **and Michael Atkinson ***

Mechanical Engineering Department, North Carolina A&T State University, Greensboro, NC 27411, USA
* Correspondence: mdatkinson@ncat.edu; Tel.: +1-(336)-285-2202

Abstract: The primary objective of this investigation was to explore the aerodynamic impact of adding trailing edge serrations to a Wells turbine. The baseline turbine consists of eight NACA 0015 blades. The blade chord length was 0.125 m and the span was 0.100 m. Two modified serrated blade configurations were studied: (1) full-span, and (2) partial-span covering 0.288c of the trailing edge. The numerical simulations were carried out by solving the three-dimensional, incompressible steady-state Reynolds Averaged Navier-Stokes (RANS) equations using the k-ω SST turbulence model in ANSYS™ (CFX). The aerodynamic performance of the modified Wells turbine was compared to the baseline by calculating non-dimensional parameters (i.e., torque coefficient, pressure drop coefficient, and turbine efficiency). A comparison of the streamlines was performed to analyze the flow topology around the turbine blades for a flow coefficient range of $0.075 \leq \phi \leq 0.275$, representing an angle of attack range of $4.29° \leq \alpha \leq 15.3°$. The trailing edge serrations generated a substantial change in surface pressure and effectively reduced the separated flow region, thus improving efficiency in most cases. As a result, there was a modest peak efficiency increase of 1.51% and 1.22%, for the partial- and full-span trailing edge serrations, respectively.

Keywords: renewable energy; wave energy conversion; CFD

1. Introduction

The negative impacts of carbon-emitting energy sources have hastened the need to develop alternative forms of energy production. The Office of Energy Efficiency & Renewable Energy reports that renewable energy accounted for approximately 20% of all U.S. electricity in 2021, and that percentage is expected to grow [1]. The International Energy Agency (IEA) is expecting the renewable capacity to increase over 8% in 2022 [2]. Popular forms of eco-friendly renewable energy include land- and sea-based solar and wind applications. Novel devices that utilize marine energy offer the possibility of harnessing the kinetic energy of ocean waves. One such design uses the oscillating water column principle and has received renewed attention. The Oscillating Water Column (OWC) is a well-studied marine renewable energy harvesting technique that has successfully produced electricity. A significant component of the conventional OWC is the Wells turbine. However, an OWC equipped with a Wells turbine has a limited operating range, low aerodynamic efficiency, high noise levels, and poor starting characteristics. Among the wide range of renewable energy sources, wave energy could become economically viable in the near future. The conversion of wave energy is an attractive proposition for countries surrounded by the sea, such as the British Isles, Japan, India, and others. Globally, ocean waves offer huge potential for harnessing energy. Locally, in the U.S., more than 50% of the population lives within 50 miles of the coast, making wave energy a logical and ideal form of power generation [3].

In the late 1970s, Prof. Alan Arthur Wells of Queen's University Belfast developed the Wells turbine, an effective air turbine used for bi-directional air flow. The Wells turbine rotor is illustrated in Figure 1. It consists of several symmetrical airfoil blades arranged

around a central hub with their chord lines normal to the rotation axis. This turbine is more efficient than other turbines because it doesn't require rectifying air valves and can extract power at low mass flow rates. An axial flow air turbine such as the Wells is considered one of the simplest and most economical ways to harness wave energy
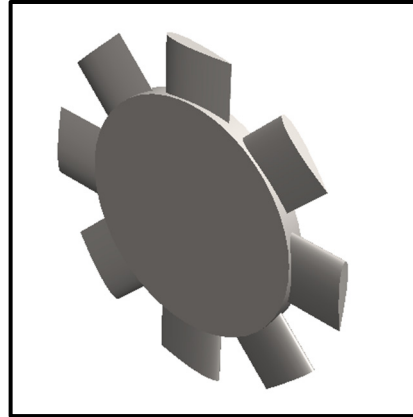
Figure 1. Wells Turbine.

It is proven that the Wells turbine is an adequate wave energy converter, even with its well-known aerodynamic performance limitations [4]. This research will investigate the aerodynamic effect of adding trailing edge serrations to Wells turbine blades.

Ocean waves create a reciprocating airflow that transfers energy to the turbine blades through the OWC. Air, which is the circulating fluid, reverses its direction with the oscillating wave (i.e., inhalation and exhalation), but the Wells turbine rotation direction remains the same. Researchers have investigated the effect of varying Wells turbine design parameters through experimental and numerical analyses. In the following section, we briefly discuss prior studies whose aim was to assess and improve its design for performance.

Using NACA0015 profiles, Ghisu et al. [5] compared experimental and numerical performance characteristics of a high-solidity Wells turbine at different non-dimensional piston frequencies. The unsteady numerical simulations were carried out using ANSYS™ Fluent, a commercial computational fluid dynamics (CFD) flow solver. The computations focused on the flow upstream and downstream of the rotor and investigated hysteresis during piston acceleration and deceleration. Examination of the flow field differences, between the intake and exhaust strokes, were result of the machine's asymmetry. Moreover, this study shows that turbine performance can be solely attributed to delays introduced by the internal flow field correlating the turbine's performance with flow parameters (i.e., velocity and pressure) near the blade. In a similar study, Ghisu et al. [6] showed that compressibility effects determine the hysteresis between acceleration and deceleration, while differences in flow parameters and secondary structures near the rotor are negligible under similar flow conditions.

Taha et al. [7] compared the performance of a NACA0020 blade profile with various uniform tip and non-uniform [8] tip clearances using CFD. The results showed that the turbine performance is significantly influenced by tip clearance. It was shown that a turbine with non-uniform tip clearance performs similarly to one that is uniform. However, a turbine with non-uniform tip clearance, however, seems to have a better overall performance. One of the most noticeable features is that a turbine with a larger tip clearance is able to operate at a greater flow rate without stalling. Additionally, this research showed that turbine performance was greatly influenced by tip leakage flow. The study concluded that increased tip clearance to chord length ratios led to reduced peak efficiency and wider stall margins of the turbine.

As part of the effort to improve Wells turbine performance, different researchers considered different methodologies. Takao et al. [9] improved the original Wells turbine design by adding end plates. Das et al. [10] obtained improvement of a Wells turbine

through an automated optimization technique using OPAL++. In this study, a turbine with a ring-type endplate was optimized using four geometric properties. The modified geometry increased the peak torque by 120%, the efficiency by 9%, and delayed the stall point. Shaaban et al. [11] used a duct geometry on Wells turbine to improve the performance by optimizing the duct geometry. By optimizing the duct geometry, turbine power and efficiency are increased by 14% and 9%, respectively. Halder et al. [12] improved the design of a Wells turbine by increasing the operating range. In order to find the optimal design, Reynolds-averaged Navier-Stokes (RANS) equations were solved and a surrogate approximation model was constructed. For this design, the peak efficiency dropped by 3.1%. However, compared to the reference case, both relative power output and relative stall point increased by 29% and 18%, respectively.

Mohamed et al. [13] studied multi-objective optimization of the turbine blade's airfoil to increase power and improve efficiency. The methodology explored using a monoplane Wells turbine with symmetric airfoil blades to optimize efficiency by increasing the tangential force. The performance of the proposed solution is demonstrated by detailed comparisons with the classical Wells turbine with symmetric airfoils. A new design of the airfoil shape increased power output by 11.3%, and efficiency by 1% throughout the operating range.

Setoguchi et al. [14] used 2-D and 3-D models with guide vanes to improve turbine performance. This study showed that design parameters as well as the nature of the flow downstream and upstream to determine the efficiency of a turbine. Furthermore, the study showed the upstream guide vanes are primarily responsible for improving the turbine running characteristic, while the downstream guide vanes are improving the turbine starting characteristic.

Halder et al. [15] completed a detailed review of Wells turbine design modifications and some key selected design changes include variation of airfoil profiles, blade sweep, pitch angle, and geometry. However, the research focused on multi-objective optimization of blade sweep. This study performed numerical analysis by solving the RANS equations and k-ω SST turbulence model for the flow field. Based on the computational results, the peak of torque coefficient was increased by 28.28% and the efficiency was decreased by 13.5%

Watterson et al. [16] studied the effect of solidity calculations on Wells turbine performance. A three-dimensional RANS flow solver was used to determine the performance of a Wells turbine. Using NACA 0015 blades, a monoplane device performance has been calculated with Reynolds number 8×10^5, tip Mach number 0.4, hub-to-tip ratio 0.6, and a tip clearance of 2%. For different blade counts, calculations were performed to study the effects of solidity. The results showed that by increasing turbine solidity and thus blade-to-blade fluid interaction, the turbine is less susceptible to stall.

In the present work, a Wells turbine blade design was changed by adding the Trailing Edge Serration (TES) patterns. Several theoretical [17,18], numerical [19], and experimental [20,21] studies have shown that TES can mitigate negative aeroacoustics impacts caused by the interaction of turbulent boundary layers at the trailing edge of the blade. The results of these studies verified the positive effect of trailing edge serrations on noise reduction. Recent studies have demonstrated that the practical implementation of the serration design alters the flow streamlines at the teeth's roots [22,23]. While trailing edge serrations reduce noise, the aerodynamic impacts on turbine performance have not been studied thoroughly.

2. Materials and Methods

In this work, we assess the aerodynamic performance of different trailing-edge serration designs, by solving the RANS equations using ANSYS™ CFX. Fourteen three-dimensional incompressible simulations were completed. The turbine's performance was evaluated by its torque coefficient, efficiency, and pressure drop coefficient under steady-state conditions. The system of equations was closed by coupling the RANS equations with the k-ω SST turbulence model. In order to ensure numerical accuracy, we used the

grid metrics carried out in previous work [24]. Furthermore, the computational model was validated by comparing the results to available numerical [25] and experimental [26] data. A summary of the grid independence study is provided below.

2.1. Geometry Modeling

A Wells turbine with symmetrical NACA 0015 airfoil blades fixed at a 90-degree staggered angle was utilized. The demonstrated turbine model consists of eight blades around the hub and perpendicular to the axial fluid flow direction. Each blade has a 0.125 m chord length, with hub and tip radius of 0.200 m and 0.300 m, respectively. To precisely assess the turbine performance, the tip clearance has been taken into consideration. For fluid flow in turbomachinery, the tip leakage flow is a significant secondary flow which was chosen to be 1% of the chord length.

The turbine rotor blade solidity is used to account for the wake effect on the blades. During the rotation of a turbine, solidity indicates the amount of obstructions in the airflow. Furthermore, it is a measurement of a turbine's blades' mutual interaction and a crucial design element for self-starting [27–31]. Solidity is constant at 0.67 which leads to having eight blades around the rotor. As a result of numerous studies [32], it has been demonstrated that this solidity value of 0.67 is highly suitable for Wells turbines. As a result of the Wells turbine's symmetry, we have thoroughly analyzed only one of its eight blades.

CFD analysis requires discretization of the governing equations. Also, consequently, discretization errors can appear in the CFD results. In numerical analysis, errors can be primarily caused by the quality of the computational grids. ANSYS meshing was used to discretize the flow domain by forming an unstructured mesh for the presented designs (see Figure 2). The boundary layer flow of the rotor blades must be sufficiently resolved to predict the dynamic stall point of a turbine. In order to accurately predict the viscous sublayer, because of their sensitivity to meshes, the k-ω SST turbulence model requires high resolution with $y^+ < 1$. Therefore, to capture the boundary layer flow, inflation layers of closely spaced hexahedrons were generated on the walls of the turbine blades.

(a) Leading Edge   **(b) Trailing Edge**
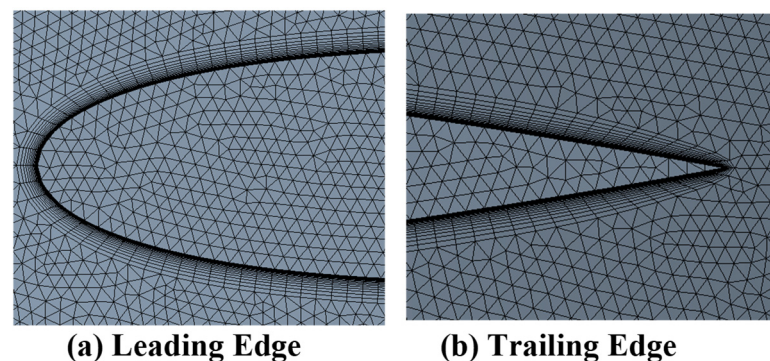
Figure 2. ANSYS Meshing Generated Around the Baseline Blade.

An inviscid flow occurs away from the airfoil surface, and a viscous flow occurs adjacent to it, where friction dissipates energy (i.e., the boundary layer). CFD has traditionally measured boundary layer thickness by δ, which is a dimensionless distance normal to the airfoil surface. By adjusting this parameter, the boundary layer develops correctly. Fluid density, absolute distance from wall, friction velocity, and viscosity are all used to calculate y^+.

$$y^+ = \frac{\rho y u_\tau}{\mu} \tag{1}$$

Based on equation or $y^+ < 1$, the first layer height was obtained as 1.1×10^{-5} with a growth factor of 1.2. The total number of inflation layers was 20. As shown below, friction velocity can be calculated using the square root of the wall shear stress to fluid density ratio.

$$u_\tau = \sqrt{\frac{\tau_w}{\rho}} \tag{2}$$

At the velocity inlet, there is a 5% turbulent intensity distributed uniformly across the velocity profile. Output boundary conditions are imposed by static pressure of 101.3 KPa at the outlet. There are four and six times the blade chord lengths upstream and downstream of the computational domain length. At the hub, tip, and blade surface, no-slip boundary conditions are specified. Considering that Wells turbines have symmetrical geometry, calculations are restricted to one blade-to-blade passage with periodic boundary conditions, as illustrated in Figure 3. Also, the turbine was set to rotate at 2000 rpm and the assigned convergence criterion for the solver was 1×10^{-5}.
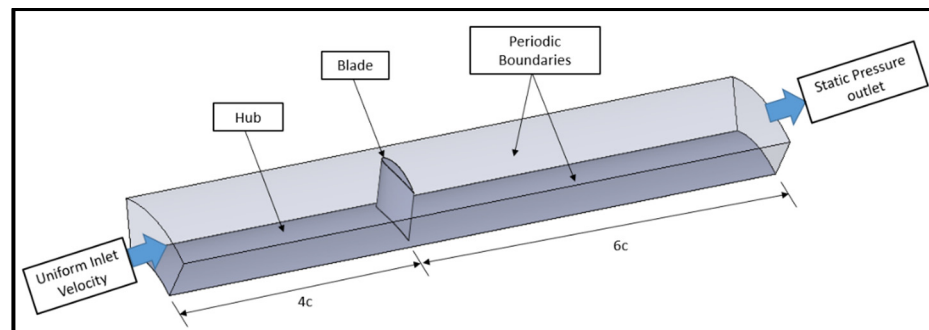
Figure 3. Computational Domain and the Boundary Conditions.

In the fluid zone, the Moving Reference Frame (MRF) rotates at a speed equivalent to the Wells turbine rotors. The governing equations incorporate centripetal and Coriolis components to take into account the MRF. ANSYS™ CFX solved the following governing equations:

The conservation of mass

$$\frac{\partial \rho}{\partial t} + \nabla . \rho \vec{v_r} = 0 \tag{3}$$

The conservation of momentum

$$\frac{\partial \left(\rho \vec{v} \right)}{\partial t} + \nabla . \left(\rho \vec{v_r} \vec{v} \right) + \rho \left[\left(\omega \hat{a} \right) \times \left(\vec{v} - \vec{v_t} \right) \right] = -\nabla p + \nabla . \tau \tag{4}$$

In this equation, $\vec{v_t}$, $\vec{v}$, ω, τ, and $\hat{a}$ respectively define transitional velocity, absolute velocity, angular velocity, viscous stress, and axis of rotation.

2.2. Grid Indepandance Study

In a prior study, four different cell-size grids were analyzed [24]. The simulations were carried out at $\phi = 0.225$ and the torque coefficient was compared. A change in grid size resulted in discrepancies of approximately 24%, 4%, and 0.5% between medium, fine, and extra-fine grids, respectively on Table 1. For the fine grid, variation in the results was negligible, resulting in reasonable accuracy. However, after examining the flow topology there was a qualitative difference between the fine and extra-fine grid. This is typical of RANS turbulence modeling of separated flows. As a result, subsequent simulations were performed using the extra-fine grids; grid dependency statistics are shown in Figure 4.

Table 1. Grid Sizes.

Mesh	No. of Grids (Millions)	Grid Size (mm)
Coarse	3.6	10.0
Medium	7.6	5.0
Fine	18.1	2.5
Extra Fine	32	1.25
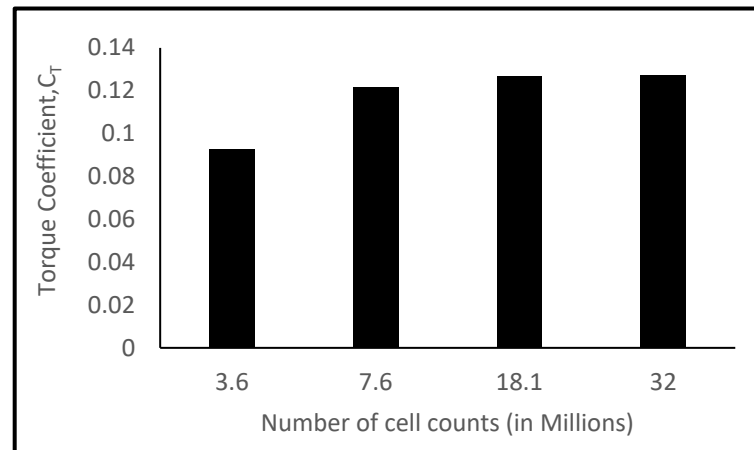
**Figure 4.** Grid Independence Study of Torque Coefficient at ϕ = 0.225.

2.3. Validation

Upon completion of the grid independence study, we compared the torque coefficient (C_T), pressure drop coefficient (ΔP_0^*), and efficiency (η) at various flow coefficients conducted in prior work [24]. As shown in Figures 5–7, the CFD results are in good agreement until the flow coefficient reached ϕ = 0.200. Here the flow coefficient is representative of a high angle of attack. Therefore, flow separation starts to form at the leading edge and causes a rapid decrease in the torque coefficient and efficiency. The numerical results deviate from the experiment because of RANS modeling inability to adequately resolve highly separated flows. Therefore, it tends to over predict torque after stall [25]. However, the present work corresponds well to other CFD results [25], given the same geometrical features.
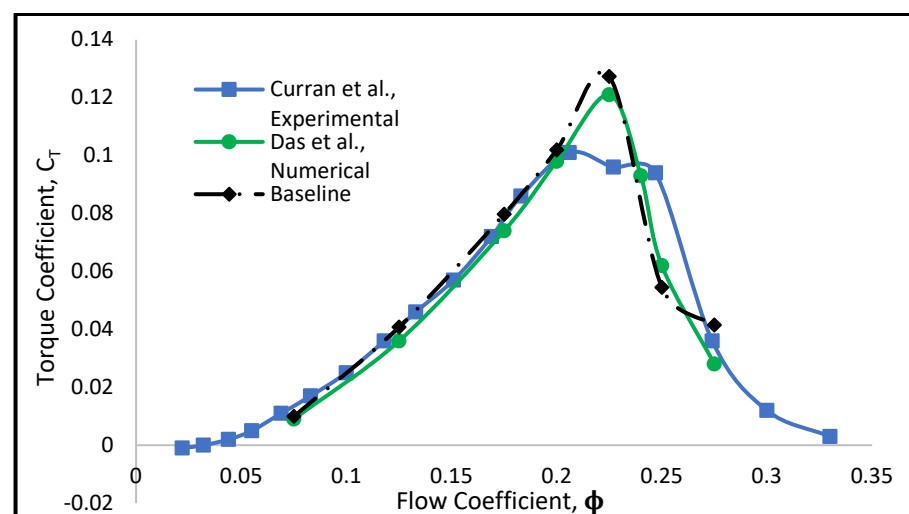
Figure 5. Comparison of numerical and experimental torque coefficient, C_T.
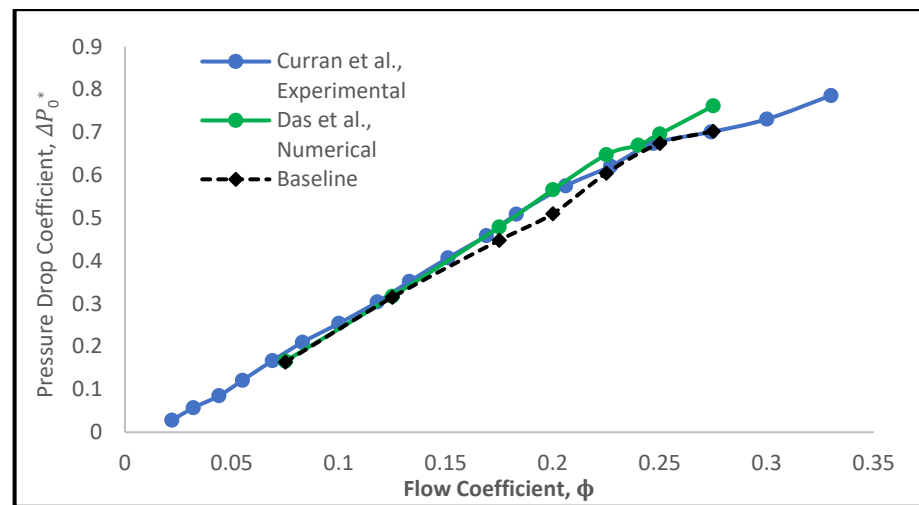
Figure 6. Comparison of numerical and experimental pressure drop coefficient, ΔP_0^*.
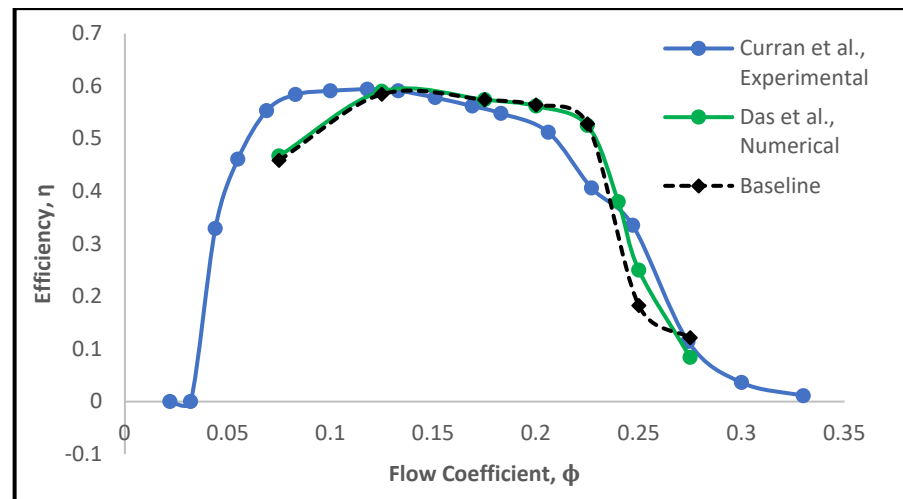
Figure 7. Comparison of numerical and experimental efficiency, η.

Traditionally, turbine performance is characterized by non-dimensional coefficients such as:

The torque coefficient, $\mathbf{C_T}$

$$\mathbf{C_T} = \frac{\mathbf{T}}{\boldsymbol{\rho}\boldsymbol{\omega}^2\mathbf{R}^5} \tag{5}$$

The Pressure drop coefficient, $\mathbf{\Delta P_0^*}$

$$\mathbf{\Delta P_0^*} = \frac{\mathbf{\Delta p_0}}{\boldsymbol{\rho}\boldsymbol{\omega}^2\mathbf{R}^2} \tag{6}$$

The efficiency, $\boldsymbol{\eta}$

$$\boldsymbol{\eta} = \frac{\mathbf{T}\boldsymbol{\omega}}{\mathbf{\Delta p_0}\mathbf{Q}} \tag{7}$$

The terms $\mathbf{T}$, $\mathbf{Q}$, $\mathbf{\Delta p_0}$, $\mathbf{U_R}$, $\mathbf{b}$, $\mathbf{c}$, $\mathbf{z}$, $\mathbf{v}$, $\boldsymbol{\omega}$, and ρ represent the blade torque, volumetric flow rate, static pressure drop across the turbine, the circumferential velocity at blade mean radius, blade height, blade chord length, number of blades, axial inlet velocity, the angular velocity of the turbine, and air density, respectively.

2.4. Serrations Setup

The modified blade model corresponds to a NACA 0015 airfoil, with chord length of c = 0.125 m and a span of L = 0.100 m. The NACA 0015 blade's profile was designed in the *x*-axis and *y*-axis, then extruded in the *z*-axis direction. The serrations were made by cutting triangular patterns on the Trailing Edge (TE) with assigned parameters. For our serration parameters, we have considered the existing modeling criterion for noise attenuation, even though we are primarily investigating the aerodynamic characteristics of the serrated trailing edges.

At a Strouhal number of $\sim$ **1** noise reduction occurs in the low-frequency region when $\frac{f\delta}{U_0} < St_\delta$. On the other hand, noise can increase when $\frac{f\delta}{U_0} > St_\delta$, reguardless of angle of attack and mean flow velocity [33]. Furthermore, according to Das et al. [25] a Wells turbine normally operates at a reduced frequency in the order of 10^{-3}, which makes it fall under the condition of $St_\delta < 1$. However, Gruber et al. [33] have considered critical values of either $\frac{h}{\delta} \sim$ **0.5** or $\frac{h}{\lambda} \sim$ **1**, beyond which significant noise reduction can occur. Our assigned serration depth, $h = $ **0.02***c* and width is $\lambda = $ **0.096***c* (See Figure 8). By the assigned dimensions; therefore, our serration pattern can meet the noise attenuation condition of:

$$\frac{h}{\delta} = 0.83 \tag{8}$$
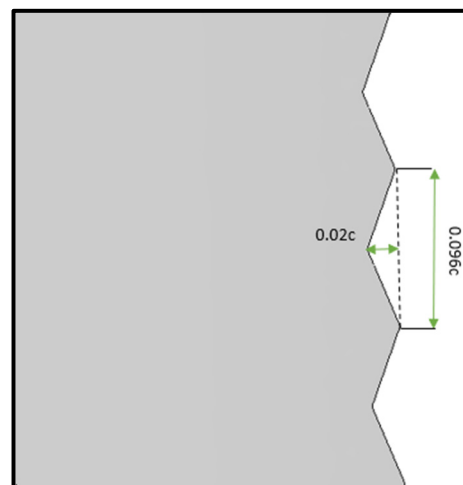
**Figure 8.** Trailing edge serration pattern of the NACA 0015 airfoil.

To obtain an optimal design of the TE serration. The first model consisted of a fully serrated trailing edge (FSTE), shown in Figure 9.
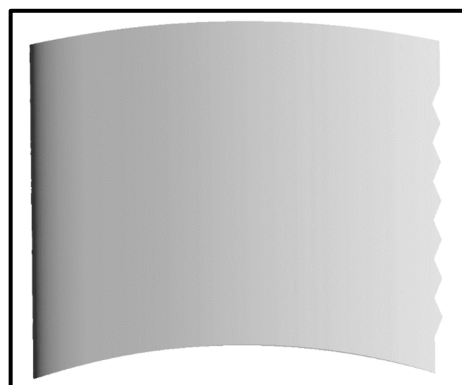
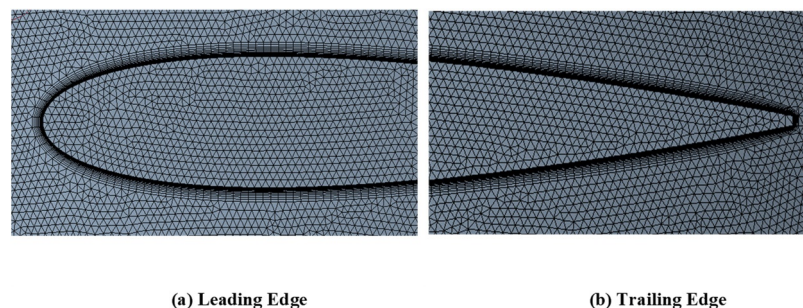**Figure 9.** Fully Serrated Trailing Edge Model on NACA0015 airfoil.

While observing the baseline turbine flow field, through range of $0.075 \leq \phi \leq 0.275$, it was observed that a small area of recirculation region begins in near hub location of the span. Therefore, we designed a second model which is a partially serrated trailing edge (PSTE), where the serration pattern covers 0.288c (36 **mm**) of the trailing edge as shown in Figure 10. Since, the serrations attenuate the noise level by mitigating the vortex shedding at the trailing edge we introduced the partial trailing edge serrations close to hub [34].
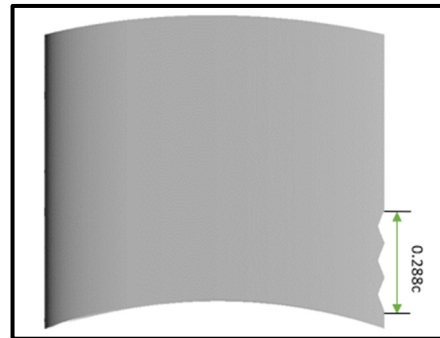
Figure 10. Partially Serrated Trailing Edge Model on NACA0015 airfoil.

After creating the serration models, the meshes were generated using ANSYS meshing by specifying same criterion as the baseline model face sizing and inflation layers. In addition, the boundary conditions remain constant for all three models. Figure 11 show the final meshing results for the fully serrated blade model. Figure 12 shows the generated mesh around the partially serrated trailing edge.

1. Fully Serrated Trailing Edge:

(a) Leading Edge (b) Trailing Edge

Figure 11. ANSYS Meshing Generated Around the Fully Serrated Blade.

2. Partially Serrated Trailing Edge:

(a) Leading Edge (b) Trailing Edge
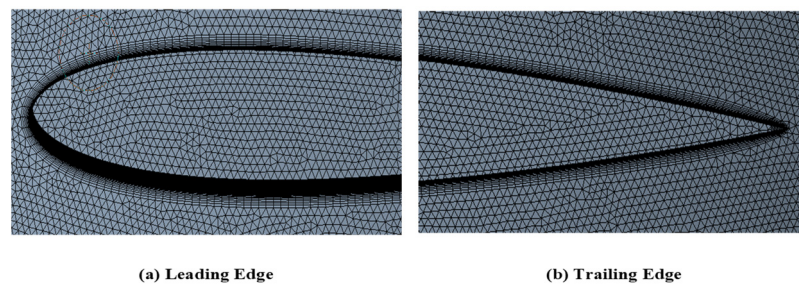
Figure 12. ANSYS Meshing Generated Around the Partially Serrated Blade.

3. Results

The CFD simulations of the modified Wells turbine were carried out at different flow coefficients that represent pre-stall, stall, and post-stall conditions. In this section, we discuss the results quantitatively and qualitatively by comparing the performance coefficients and flow topology to the baseline configuration.

3.1. Comparison of Performance Coefficients and Turbine Efficiency

The baseline has the highest torque coefficient prior to the stall point followed by the PSTE design. From Figure 13, it is shown, for all three designs, that the torque coefficient increases up to $\phi = 0.225$, from there it decreases. Hence, the turbine blades stall at a flow coefficient of 0.250, i.e., angle of attack of 14.03°. Mostly, the FSTE design produced lower torque compared to the other designs, except for, $\phi = 0.200$. This may be a result of the presence of flow separation closer to the hub and trailing edge, unlike the baseline and PSTE models. The PSTE mostly produced higher torque compared to the FSTE and lower torque compared to the baseline blade.
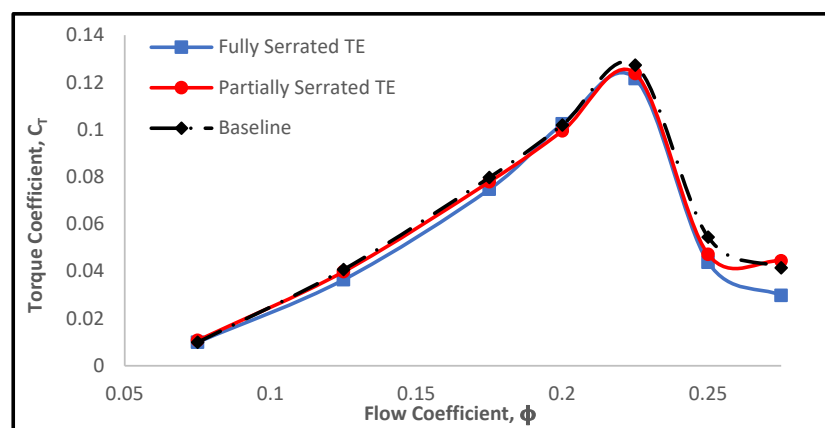

Figure 13. Torque Coefficient, C_T.

Figure 14 shows a comparison of the pressure drop across the turbine. Here the results show a linear increase with an increasing flow coefficient. The reference (i.e., baseline) case has a higher pressure drop coefficient for our range of ϕ, the FSTE has the lowest, while the PSTE design fluctuates between the baseline and FSTE configuration.
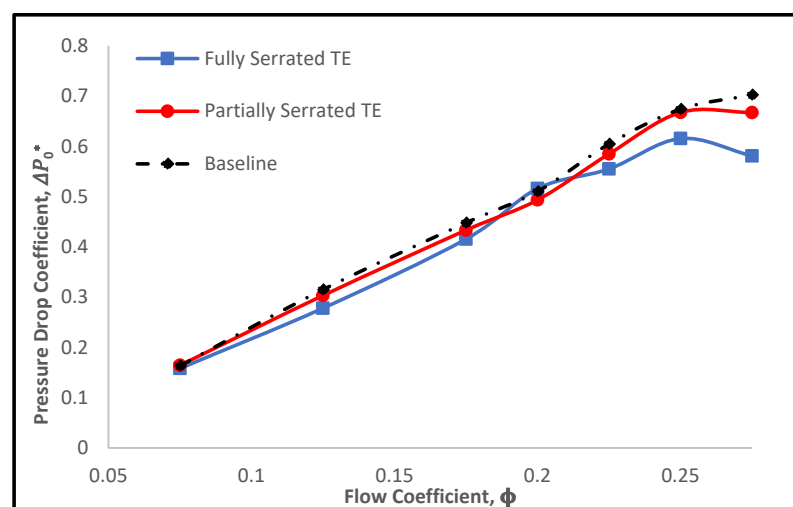

Figure 14. Pressure Drop Coefficient, ΔP_0^*.

The efficiency plot, shown in Figure 15, shows that the PSTE has the highest efficiency prior to the stall condition. PSTE increases the efficiency at the peak point by 1.51%. Secondly, the FSTE model shows a 1.22% improvement in peak efficiency compared to the baseline model. At the stall point, flow recirculation appears and more negatively impacts the serrated models. Therefore, at $\phi = 0.250$, the baseline model is more efficient because the serration pattern allows the air on the pressure side to bleed to the low-pressure suction side.
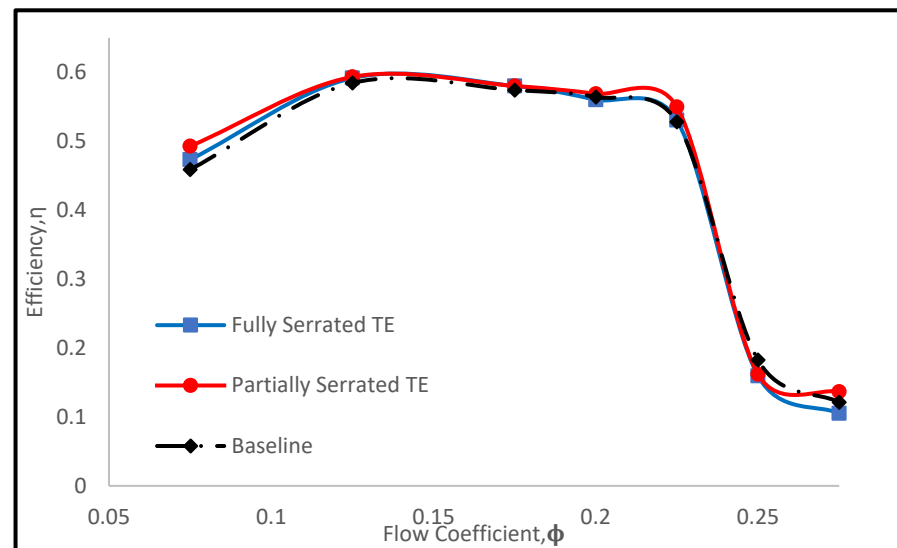
Figure 15. Efficiency, η.

3.2. Comparison of Flow Topology and Pressure Coefficient

Discussed in this section are the differences in the pressure distribution between the baseline and serrated blades at pre-stall, $\phi = 0.225$, stall, $\phi = 0.250$, and post-stall, $\phi = 0.275$ points. This section studies the flow field behavior by describing sectional views (see Figure 16) of the streamlines, C_p contours, and C_p plots at different span locations.
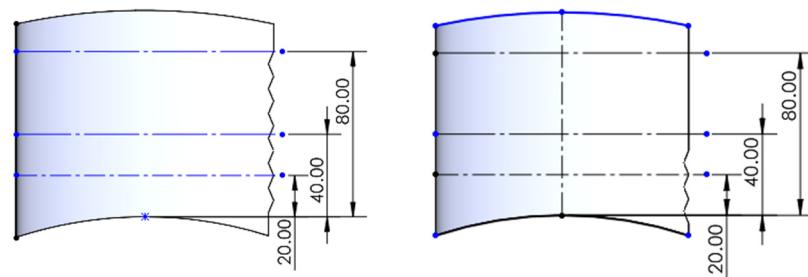

Figure 16. Sectional plane locations for FSTE on the right side, and PSTE on the left side. Pre-Stall, $\phi = 0.225$.

Figure 17 shows the streamlines at $\phi = 0.225$. We observe that the streamlines start to detach across the span near the trailing edge. For the serrated models, the saw-tooth trailing edge reduces the strength of the trailing edge wake and encourages upstream mixing and induces separation near the hub. For the FSTE, at the near-hub location, the flow bleeds over on to the suction side from the higher-pressure side [Figure 17]. Further from the hub, the flow detaches near the trailing edge at the mid- and near-tip locations for all configurations. For the PSTE configuration, while not as substantial as the FSTE, the flow moves to the suction side near-hub and reattaches on the suction side and reduces the size of the wake, but results in induced separation on the suction side, thus reducing torque. However, due to a lower pressure drop for the serrated configurations, there is a

modest improvement in efficiency. The PSTE has higher efficiency compared to the FSTE configuration because the flow attaches closer to the TE.
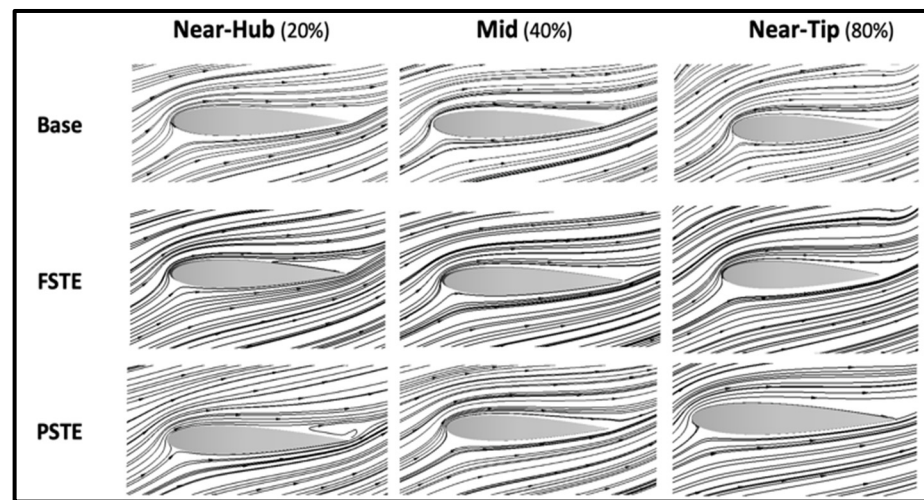

Figure 17. Streamlines at ϕ = 0.225.

Figure 18 presents the C_p contours of three models along the span. The baseline model has the largest low-pressure zone close to the leading edge on the suction side. We observe higher pressure starting to bleed onto the suction side at the mid-span location. The FSTE configuration has the largest suction side trailing edge low-pressure zone among the presented designs. Creating lower pressure on the suction side is undesired in this case because it reduces the aerodynamic performance of the turbine. Additionally, the FSTE design creates a large adverse pressure gradient which leads to flow separation. It can be shown that the FSTE model shows greater bleed compared to the other designs. The PSTE decreased the bleed of air from the pressure to the suction side at the trailing edge.
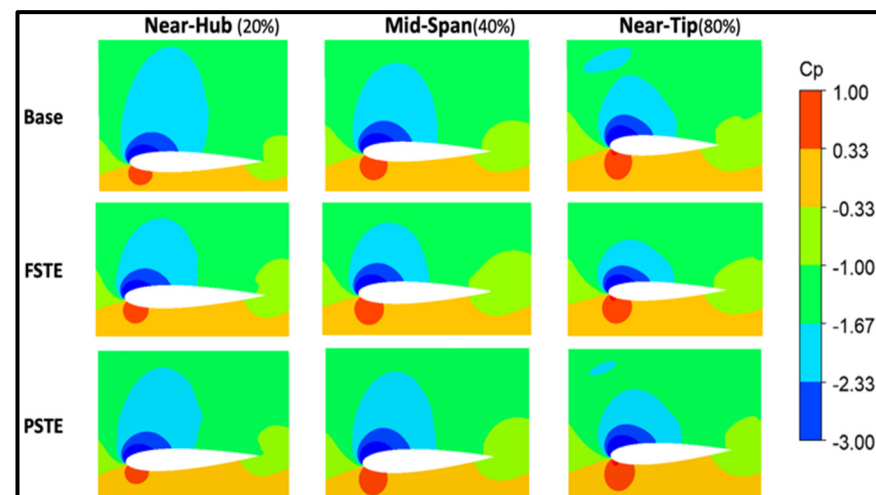

Figure 18. Contours of C_p. for ϕ = 0.225.

The fully serrated trailing edge has a higher-pressure gradient at the trailing edge because of the flow bleeding from the pressure side to the suction side, as shown in Figure 19. Further, the high-pressure gradient at the trailing edge acts as resistance to turbine rotation which is responsible for lower torque generation. Therefore, the FSTE model has the lowest efficiency.

At the stall point, ϕ = 0.250, a recirculation zone appears, for all models, as shown in Figure 20. For the baseline configuration, recirculation appears near the mid-span at the trailing edge. Near the tip location, the recirculation has increased in size and moved

towards the leading edge. For the FSTE model, minor recirculation is observed at the near hub and becomes larger at the mid-span of the trailing edge. At the near tip location, the recirculation field moved towards the leading edge. The PSTE model, recirculation appears near the hub due to the higher pressure at the trailing edge. At the near-tip location, the circulation is close to the leading edge similar to the baseline model.
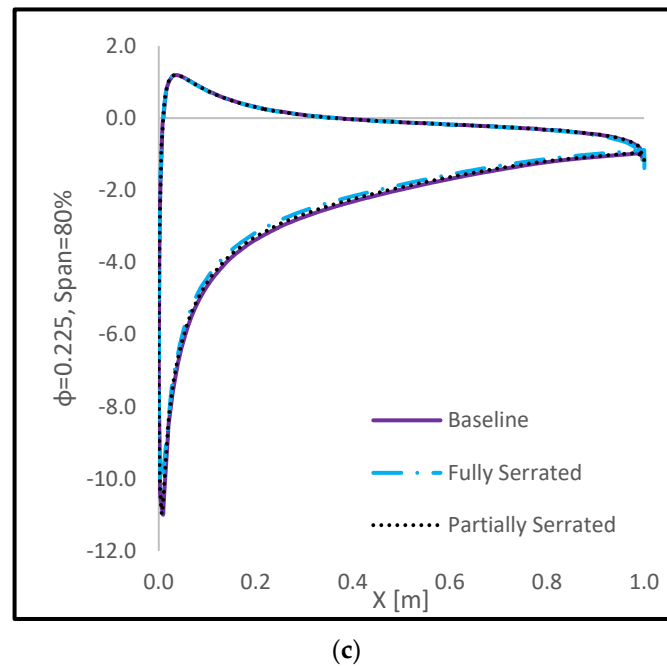
(**a**)

(**b**)

Figure 19. *Cont.*

(c)
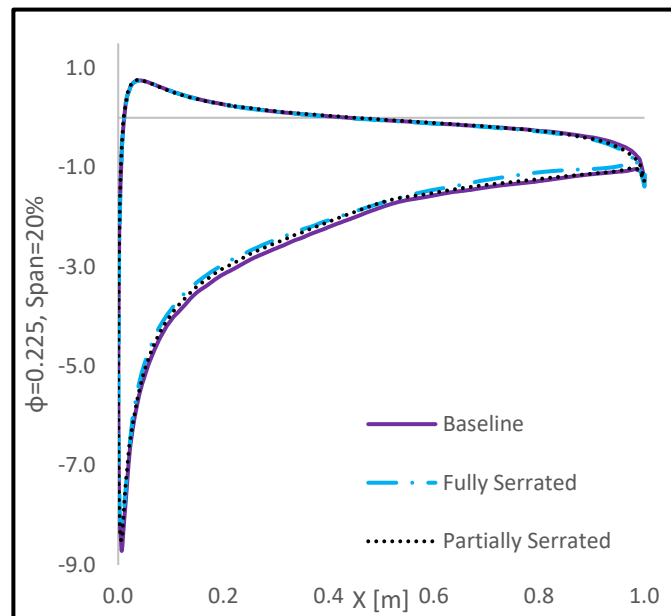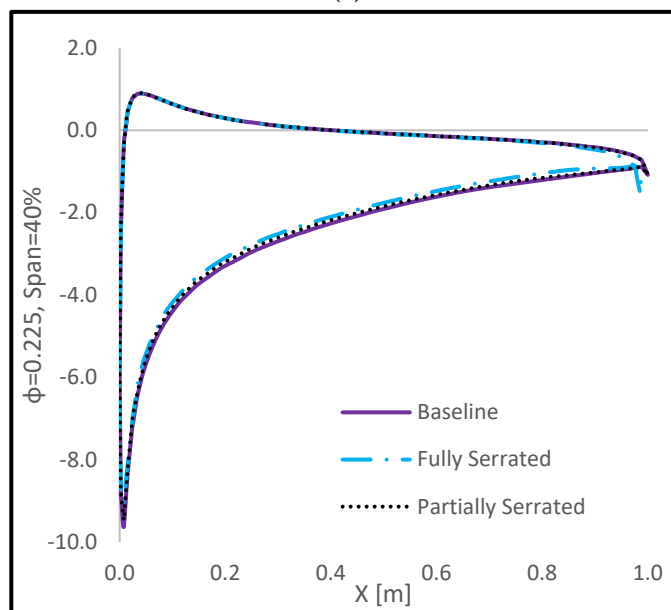
Figure 19. Plot of C_P, $\phi = 0.225$. (**a**) 20% span, (**b**) 40% span, (**c**) 80% span. Stall, $\phi = 0.250$.
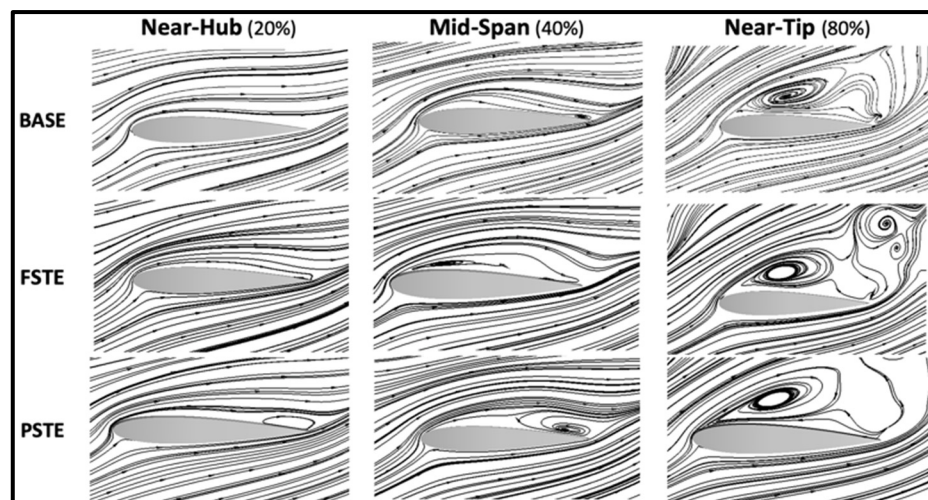

Figure 20. Streamlines at $\phi = 0.250$.

Figure 21 presents the C_p contours at the stalling point for all designs. It can be shown that the baseline model has a greater lower pressure region across the chord compared to the pre-stall condition. This low-pressure creates suction and causes a recirculation zone by attracting the higher-pressure trailing edge fluid thus leading to stall. Due to the partial span serrations of the PSTE, has a localized low-pressure zone near-hub compared to the other designs as shown in Figure 21. As a result, it has minor recirculation at the trailing edge due to bleed from the pressure side. Near the mid-span location, unlike the previous locations, the FSTE model has two distinct low-pressure zones distributed close to the leading and trailing edges on the suction side of the blade. Therefore, at the near mid-span location, this design tends to have multiple recirculation zones. The PSTE model has a greater lower pressure zone compared to the pre-stall condition. Recirculation appeared starting at the near-hub location. The flow detached near the mid-span due to higher pressure around the trailing edge. Near-tip, the lower pressure zone increased which allows additional high-pressure air to bleed onto the suction side.
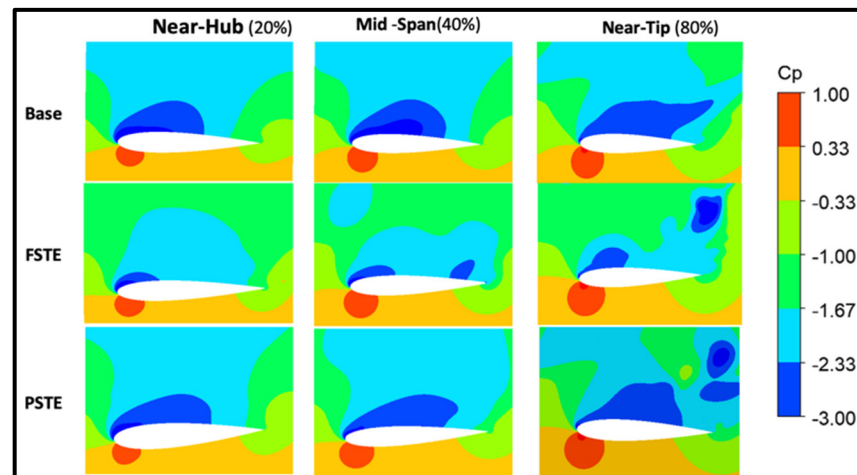
Figure 21. Contours of C_p. for ϕ = 0.250. 20% span, 40% span, 80% span.

The FSTE model reduced the low-pressure region along the suction side of the blade. This is shown in Figure 22. The C_p plots clearly show higher suction side pressure that results in a reduction of pressure drop and torque coefficient. However, this results in a slight improvement of efficiency. At the near-hub, the PSTE demonstrates better performance even though there is evidence of trailing edge separation. Due to the serrations, the pressure drop is less severe compared to the baseline configuration, thus improving efficiency. However, at the near mid-span location, the low-pressure zone extends approximately 80% of the airfoil which possibly represents the turbine experiencing stall sooner than the other configurations. Again, the low-pressure zone appears at 80% chord and continues until the trailing edge causing a large recirculation zone for the FSTE. As a result, the FSTE produced the lowest aerodynamic performance. When it comes to the near-tip location, the baseline and PSTE models show similar trends. Although, the low-pressure region is slightly higher for the baseline, near the leading edge, up to the mid-chord position. From 30% of the chord to the near trailing edge, the FSTE has the smallest pressure gradient. However, at the trailing edge, the FSTE model has the highest flow bleed resulting in less torque and lower efficiency.

In the end, the post-stall condition, ϕ = 0.275, is shown in Figure 23. The baseline model, near-hub, does not have recirculation but at the near mid-span recirculation appears. Also, near-tip, the flow is highly separated, and a recirculation zone appears. For the FSTE model, recirculation appeared at all observed span locations. The recirculation at the mid-span has increased in size and shows substantial flow separation near the trailing edge. The PSTE model, shows no detached flow near the hub; however, recirculation appears near the mid-span on the leading and trailing edges. Lastly, even though the near tip location shows less recirculation for the PSTE model, the turbine is fully stalled.

Figure 24 presents the C_p contours for the post-stall condition. It is obvious that the lower pressure region has expanded for all three models compared to previous angles of attack (i.e., flow coefficient). By increasing the lower pressure area, the suction of higher-pressure flow will increase, as a result, multiple recirculation zones are observed.

The FSTE model produced the lowest suction side pressure on the airfoil, except at the trailing edge, for all the span locations [Figure 25]. At the near-hub location, the PSTE demonstrates better performance regarding flow separation compared to the FSTE and baseline models. However, at the near mid-span location, the low-pressure zone for the baseline configuration extends to around 80% of the airfoil chord which typically represents turbine stall. Again, the low-pressure zone appears at 80% of the chord and extends to the trailing edge which causes huge recirculation in the FSTE model. As a result, the FSTE showed the lowest aerodynamic performance. When it comes to the near-tip location, the baseline and PSTE models show similar trends. Although, the low-pressure region is

slightly higher for the baseline model near the leading edge up to the mid-chord. From the airfoil chord position of 30% to near the trailing edge, the FSTE model has the smallest pressure gradient. However, at the trailing edge FSTE model, the flow bleed causes less torque production and lower efficiency.
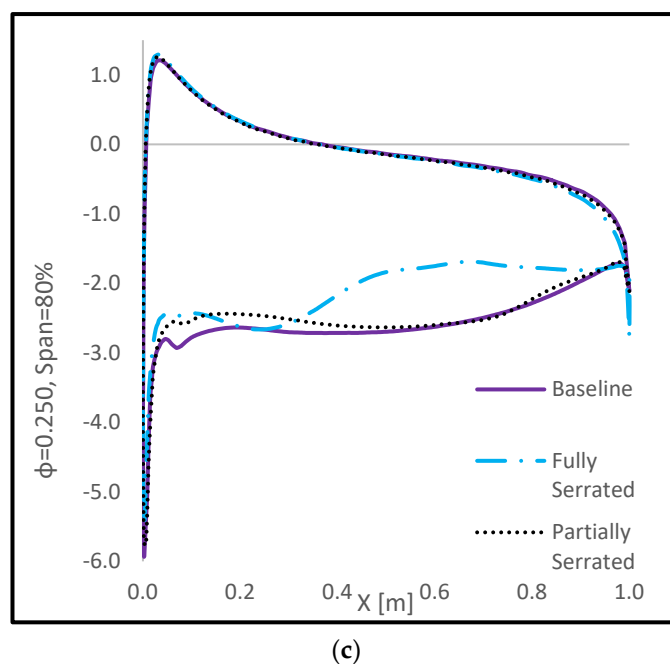

(a)

(b)

Figure 22. *Cont*.

(**c**)
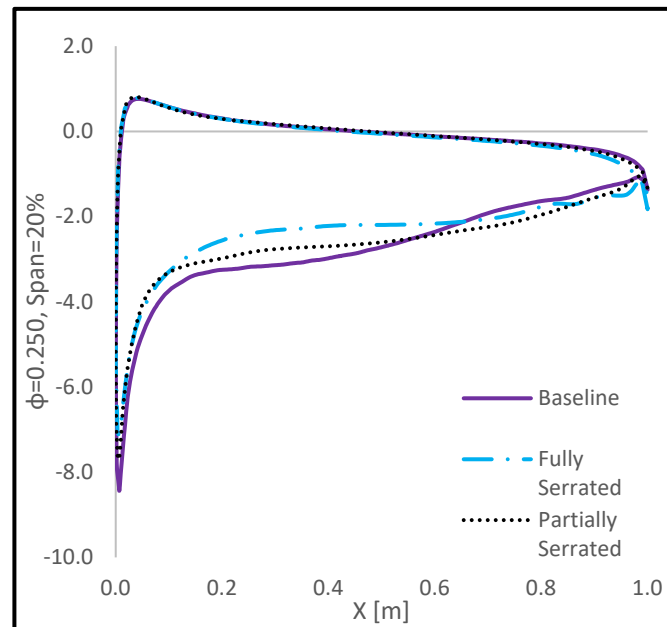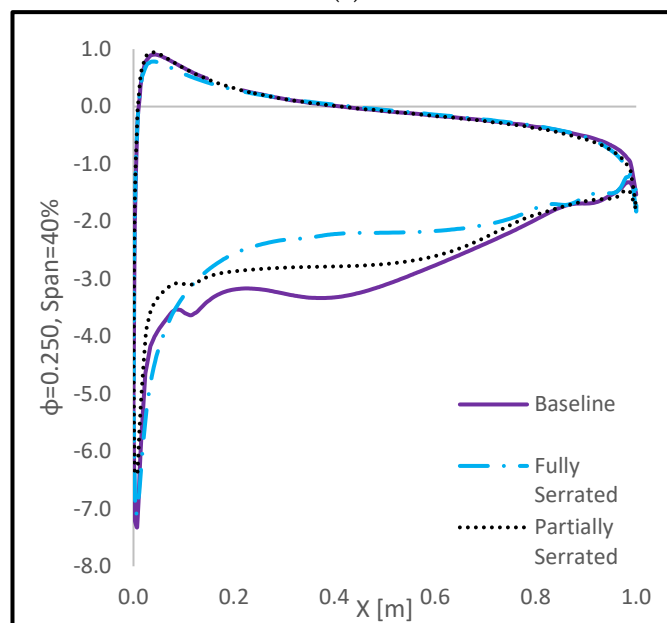
Figure 22. Plot of C_P, ϕ = 0.250. (**a**) 20% span, (**b**) 40% span, (**c**) 80% span. Post-Stall, ϕ = 0.275.
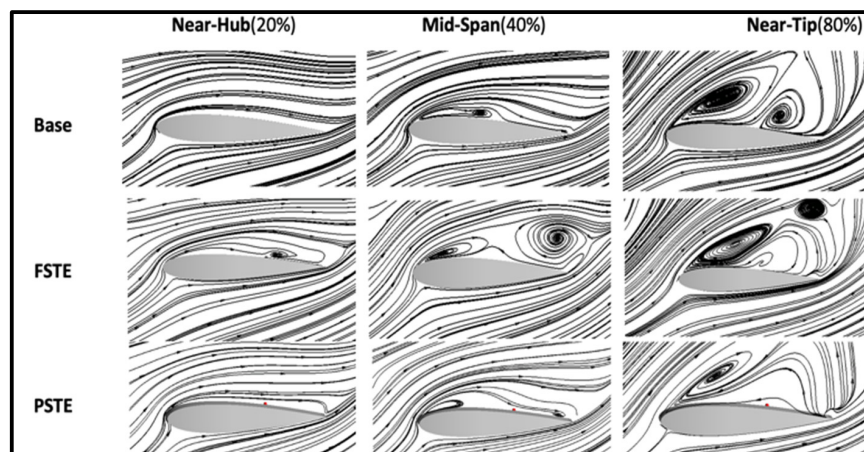

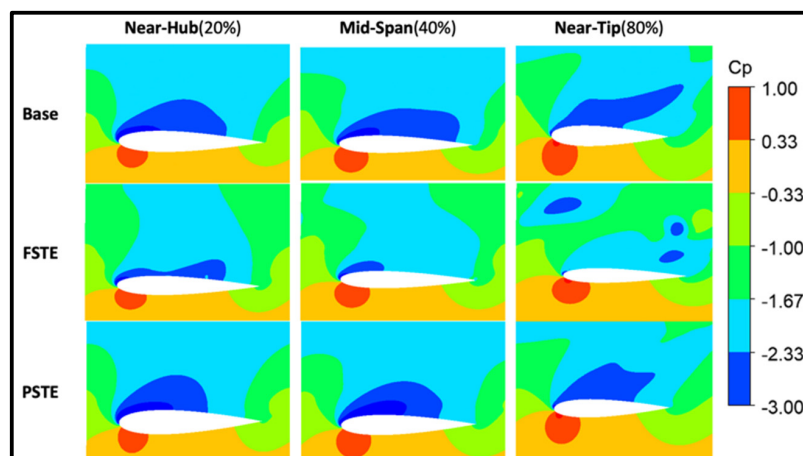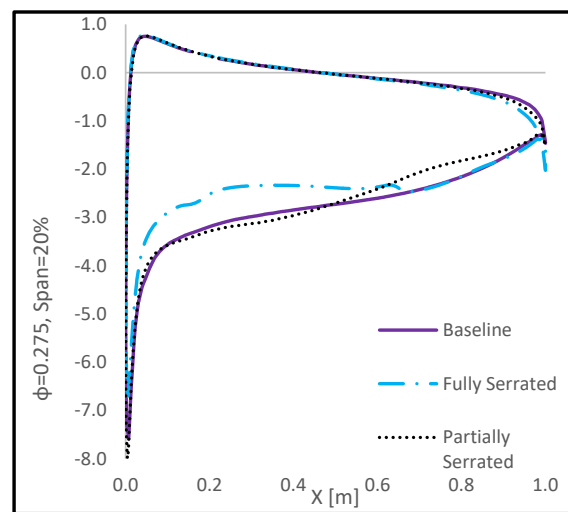**Figure 23.** Streamlines at the post-stall condition, ϕ = 0.275.
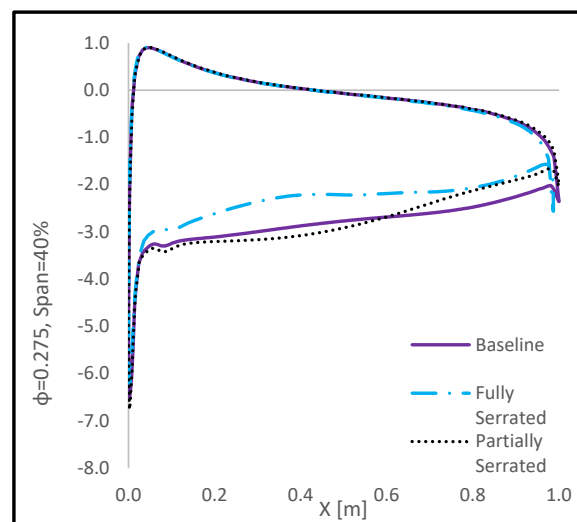

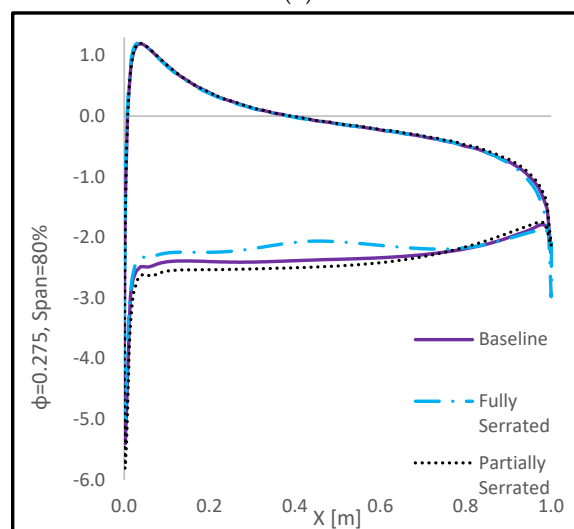**Figure 24.** Contours of C_P. for ϕ = 0.275.

Figure 25. Plot of C$_P$, φ = 0.275. (**a**) 20% span, (**b**) 40% span, (**c**) 80% span.

4. Discussion

This study investigated the influence of trailing edge serrations on a NACA- 0015 Wells turbine. Two serration patterns were explored: (1) a fully-serrated trailing edge, and (2) a partially-serrated trailing edge. The flow topology and aerodynamic performance were assessed and compared to a baseline (non-serrated) NACA 0015 airfoil at varying flow coefficients. Three-dimensional incompressible RANS simulations showed that the PSTE model has the highest efficiency under unstalled conditions. Also, at low flow coefficients, the PSTE increases the peak efficiency by 1.51%; The FSTE had a 1.22% increase. Due to massive flow separation close to the stall point, the RANS solver overpredicts torque. This is typical of such turbulence models and it is notoriously difficult to resolve such flow fields. Furthermore, our results are consistent with other numerical simulations. However, at unstalled conditions the solver computes accurate results and demonstrates good agreement with the experimental data for $\phi \leq 0.200$. Because the efficiency improves in the range where the solver shows excellent agreement, we can say that the computed results are accurate and show a modest improvement. The FSTE and PSTE designs tend to have a high degree of trailing edge induced separation due to higher air bleed, thus resulting in reduced torque. This results in a reduced pressure drop and in a modest increase in efficiency. Future studies should include higher-fidelity simulations to resolve the highly separated flow. Furthermore, as the PSTE model a have higher peak efficiency, parametric studies and shape optimization of the turbine blades with partial serrations should be explored to determine the impact on turbine performance. Variation of serration dimensions and locations can be studied to determine the optimum partial serration pattern.

Author Contributions: Conceptualization, A.S.A., M.A. and M.N.U.; methodology, A.S.A.; software, A.S.A.; validation, M.N.U. and A.A.; formal analysis, A.S.A.; investigation, A.S.A.; resources, M.A.; data curation, A.S.A. and M.N.U.; writing—original draft preparation, A.S.A.; writing—review and editing, A.S.A., M.N.U. and M.A.; visualization, A.S.A.; supervision, M.A.; project administration, M.A.; funding acquisition, M.A. All authors have read and agreed to the published version of the manuscript.

Institutional Review Board Statement: Not applicable.

Informed Consent Statement: Not applicable.

Data Availability Statement: Not applicable.

Nomenclature

a	acceleration (m/s^2)
τ	shear stress
ρ	density (kg/m^3)
c	chord length (m)
C_T	torque coefficient
λ	nondimensional width
h	nondimensional depth
St_δ	Strouhal number
L	length scale (m)
Δp_0	static pressure drop (Pa)
$\mathbf{\Delta P_0^*}$	pressure drop coefficient
Q	volumetric flow rate (m^3/s)
R	rotor radius (m)
Re	Reynolds number
T	blade torque (Nm)

$\mathbf{u_t}$	friction velocity (m/s)
v	axial velocity (m/s)
y	first layer distance from the wall (m)
$\mathbf{y}^{+}$	dimensionless wall distance
f	frequency
$\boldsymbol{\nu_t}$	turbulent viscosity (kg/m-s)
φ	flow coefficient
η	efficiency
μ	dynamic viscosity (Ns/m^2)
ω	angular velocity (rad/s)
δ	boundary layer thickness (m)

References

1. EIA Expects Renewables to Account for 22% of U.S. Electricity Generation in 2022. Available online: https://www.eia.gov/todayinenergy/detail.php?id=53459 (accessed on 2 November 2022).
2. Renewable Energy Market Update—May 2022—Analysis, IEA. Available online: https://www.iea.org/reports/renewable-energy-market-update-may-2022 (accessed on 2 November 2022).
3. Marine Energy Basics. Energy.gov. Available online: https://www.energy.gov/eere/water/marine-energy-basics (accessed on 2 November 2022).
4. Lekube, J.; Garrido, A.J.; Garrido, I.; Otaola, E.; Maseda, J. Flow Control in Wells Turbines for Harnessing Maximum Wave Power. *Sensors* **2018**, *18*, 535. [CrossRef]
5. Ghisu, T.; Puddu, P.; Cambuli, F. Numerical analysis of a wells turbine at different non-dimensional piston frequencies. *J. Therm. Sci.* **2015**, *24*, 535–543. [CrossRef]
6. Ghisu, T.; Puddu, P.; Cambuli, F. A detailed analysis of the unsteady flow within a Wells turbine. *Proc. Inst. Mech. Eng. Part A J. Power Energy* **2017**, *231*, 197–214. [CrossRef]
7. Taha, Z.; Sawada, T. A comparison of computational and experimental results of Wells turbine performance for wave energy conversion. *Appl. Ocean Res.* **2010**, *32*, 83–90. [CrossRef]
8. Taha, Z.; Ya, T.T.; Sawada, T. Numerical investigation on the performance of Wells turbine with non-uniform tip clearance for wave energy conversion. *Appl. Ocean Res.* **2011**, *33*, 321–331. [CrossRef]
9. Takao, M.; Setoguchi, T.; Kinoue, Y.; Kaneko, K. Wells Turbine with End Plates for Wave Energy Conversion. *Ocean Eng.* **2007**, *34*, 1790–1795. [CrossRef]
10. Das, T.K.; Kerikous, E.; Venkatesan, N.; Janiga, G.; Thevenin, D.; Samad, A. Performance Improvement of a Wells Turbine through an Automated Optimization Technique. *Energy Convers. Manag. X* **2022**, *16*, 100285. [CrossRef]
11. Shaaban, S.; Hafiz, A.A. Effect of duct geometry on Wells turbine performance. *Energy Convers. Manag.* **2012**, *61*, 51–58. [CrossRef]
12. Halder, P.; Samad, A.; Thévenin, D. Improved design of a Wells turbine for higher operating range. *Renew. Energy* **2017**, *106*, 122–134. [CrossRef]
13. Mohamed, M.; Janiga, G.; Pap, E.; Thévenin, D. Multi-objective optimization of the airfoil shape of Wells turbine used for wave energy conversion. *Energy* **2011**, *36*, 438–446. [CrossRef]
14. Setoguchi, T.; Santhakumar, S.; Takao, M.; Kim, T.; Kaneko, K. Effect of guide vane shape on the performance of a Wells turbine. *Renew. Energy* **2001**, *23*, 1–15. [CrossRef]
15. Halder, P.; Rhee, S.H.; Samad, A. Numerical optimization of Wells turbine for wave energy extraction. *Int. J. Nav. Arch. Ocean Eng.* **2017**, *9*, 11–24. [CrossRef]
16. Watterson, J.K.; Raghunathan, S. Computed Effects of Solidity on Wells Turbine Performance. *JSME Int. J. Ser. B* **1998**, *41*, 177–183. [CrossRef]
17. Howe, M. A review of the theory of trailing edge noise. *J. Sound Vib.* **1978**, *61*, 437–465. [CrossRef]
18. Howe, M. Aerodynamic noise of a serrated trailing edge. *J. Fluids Struct.* **1991**, *5*, 33–45. [CrossRef]
19. Jones, L.; Sandberg, R. *Direct Numerical Simulations of Noise Generated by the Flow over an Airfoil with Trailing Edge Serrations*; American Institute of Aeronautics and Astronautics: Reston, VA, USA, 2009. [CrossRef]
20. Oerlemans, S.; Fisher, M.; Maeder, T.; Kögler, K. Reduction of Wind Turbine Noise Using Optimized Airfoils and Trailing-Edge Serrations. *AIAA J.* **2009**, *47*, 1470–1481. [CrossRef]
21. Gruber, M.; Azarpeyvand, M.; Joseph, P.F. Airfoil Trailing Edge Noise Reduction by the Introduction of Sawtooth and Slitted Trailing Edge Geometries. In Proceedings of the 20th International Congress on Acoustics, Sydney, Australia, 23–27 August 2010; p. 9.
22. Ragni, D.; Avallone, F.; van der Velden, W.C.P.; Casalino, D. Measurements of near-wall pressure fluctuations for trailing-edge serrations and slits. *Exp. Fluids* **2018**, *60*, 6. [CrossRef]
23. Avallone, F.; Arce León, C.; Pröbsting, S.; Lynch, K.; Ragni, D. Tomographic-PIV Investigation of the Flow over Serrated Trailing-Edges. In Proceedings of the 54th AIAA Aerospace Sciences Meeting, San Diego, CA, USA, 4–8 January 2016.
24. Uddin, M.N.; Atkinson, M.; Das, T.K.; Esau, S. *Computational Fluid Dynamics Investigation of a Novel Bi-Directional Axial Flow Turbine for Wave Energy Conversion*; American Institute of Aeronautics and Astronautics: Reston, VA, USA, 2022. [CrossRef]
25. Das, T.K.; Samad, A. Influence of stall fences on the performance of Wells turbine. *Energy* **2019**, *194*, 116864. [CrossRef]

26. Curran, R.; Gato, L. The energy conversion performance of several types of Wells turbine designs. *Proc. Inst. Mech. Eng. Part A J. Power Energy* **1997**, *211*, 133–145. [CrossRef]
27. Liu, Z. Self-Starting Analysis of an OWC Axial Impulse Turbine in Constant Flows: Experimental and Numerical Studies. *Appl. Ocean Res.* **2018**, *82*, 458–469.
28. Raghunathan, S. The wells air turbine for wave energy conversion. *Prog. Aerosp. Sci.* **1995**, *31*, 335–386. [CrossRef]
29. Raghunathan, S.; Tan, C.P.; Wells, N. Wind Tunnel Tests on Airfoils in Tandem Cascade. *AIAA J.* **1981**, *19*, 1490–1492. [CrossRef]
30. Raghunathan, S.; Tan, C. Aerodynamic performance of a Wells air turbine. *J. Energy* **1983**, *7*, 226–230. [CrossRef]
31. Suzuki, M.; Arakawa, C.; Tagori, T. Fundamental Studies on Wells Turbine for Wave Power Generator; 1st Report, The Effect of Solidity, and Self-Starting. *Bull. JSME* **1984**, *27*, 1925–1931. [CrossRef]
32. Setoguchi, T.; Santhakumar, S.; Takao, M.; Kim, T.; Kaneko, K. A modified Wells turbine for wave energy conversion. *Renew. Energy* **2003**, *28*, 79–91. [CrossRef]
33. Gruber, M.; Joseph, P.; Chong, T. On the Mechanisms of Serrated Airfoil Trailing Edge Noise Reduction. In Proceedings of the 17th AIAA/CEAS Aeroacoustics Conference (32nd AIAA Aeroacoustics Conference), Portland, OR, USA, 5–8 June 2011; American Institute of Aeronautics and Astronautics: Reston, VA, USA, 2011.
34. Intravartolo, N.; Sorrells, T.; Ashkharian, N.; Kim, R. Attenuation of Vortex Noise Generated by UAV Propellers at Low Reynolds Numbers. In Proceedings of the 55th AIAA Aerospace Sciences Meeting, Grapevine, TX, USA, 9–13 January 2017; American Institute of Aeronautics and Astronautics: Reston, VA, USA, 2017.